Advanced Characterization of 1 eV GaInAs Inverted Metamorphic Solar Cells

Beatriz Galiana [1,*], **Amalia Navarro** [1], **Manuel Hinojosa** [2], **Ivan Garcia** [2], **Diego Martin-Martin** [3], **Juan Jiménez** [4] **and Elisa García-Tabarés** [1]

[1] Physics Department, Universidad Carlos III de Madrid (UC3M), Av. Universidad 40, 28911 Leganés, Spain; amnavarr@fis.uc3m.es (A.N.)

[2] Solar Energy Institute, Universidad Politécnica de Madrid (IES-UPM), Av. Complutense s/n, 28040 Madrid, Spain

[3] Departamental II, Universidad Rey Juan Carlos, C. Tulipán, s/n, 28933 Móstoles, Spain

[4] GdS Optronlab, Universidad de Valladolid (UVA), Paseo de Belén 11, 47011 Valladolid, Spain

[*] Correspondence: bgaliana@fis.uc3m.es; Tel.: +34-916246261

Abstract: In this work, 1 eV $Ga_{0.7}In_{0.3}As$ inverted metamorphic (IMM) solar cells were analyzed to achieve a deeper understanding of the mechanism limiting their improvement. For this purpose, high-resolution X-ray diffraction (HRXRD), transmission electron microscopy (TEM), high-resolution cross-sectional cathodoluminescence (CL), and transient in situ surface reflectance were carried out. Additionally, the photovoltaic responses of the complete devices were measured using the external quantum efficiency (EQE) and numerically simulated through Silvaco TCAD ATLAS. The combination of structural characterization of the semiconductor layers and measurements of the solar cell photovoltaic behavior, together with device modeling, allows us to conclude that the lifetime of the bulk minority carriers is the limiting factor influencing the PV response since the recombination at the interfaces (GaInP window–GaInAs emitter and GaInAs base–GaInP back surface field (BSF)) does not impact the carrier recombination due to the favorable alignment between the conduction and the valance bands. The advanced characterization using cross-sectional cathodoluminescence, together with transient in situ surface reflectance, allowed the rejection of the formation of traps related to the GaInAs growth conditions as being responsible for the decrement in the minority-carrier lifetime. Conversely, the TEM and HRXRD revealed that the presence of misfit dislocations in the GaInAs layer linked to strain relaxation, which were probably formed due to an excessive tensile strain in the virtual substrate or an incorrect combination of alloy compositions in the topmost layers, was the dominant factor influencing the GaInAs layer's quality. These results allow an understanding of the contributions of each characterization technique in the analysis of multi-junction solar cells.

Keywords: inverted metamorphic solar cells; III-V semiconductors; transmission electron microscopy (TEM); high-resolution cross-sectional cathodoluminescence (CL)

1. Introduction

Multi-junction solar cells (MJSCs) based on III-V semiconductors are currently the most promising approach to achieving high-efficiency solar cells for concentrator, area-constrained, and lightweight applications. Most commercial concentrator systems use lattice-matched $Ga_{0.5}In_{0.5}P/Ga_{0.99}In_{0.01}As/Ge$ triple-junction solar cells, which show efficiencies of 38–40% and a lab record of 41.6% [1]. This architecture cannot be increased significantly above 40% mainly due to the fact that the Ge sub-cell (0.67 eV) absorbs approximately twice the number of low-energy photons than what is needed for current matching using the $Ga_{0.5}In_{0.5}P$ (1.8 eV) and GaAs (1.44 eV) sub-cells, thus implying an excess current that is not harnessed together with a lower voltage than could be obtained with a proper bandgap sub-cell for the bottom cell [2].

Several improved architectures to go a step further rely on atomic-scale material design for MJSCs. Some recent approaches are based on the use of thick GaInAs/GaAsP strain-balanced quantum well (QW) solar cells to improve current matching in triple-junction solar cells, achieving 39.5% terrestrial and 34.2% space efficiency [3]. Also, the number of junctions can be increased, with a 47.1% conversion efficiency obtained under a 143 Suns concentration with six junctions [4].

The architecture studied in this work is based on the development of a triple-junction solar cell that replaces the Ge bottom cell (0.67 eV) with a $Ga_{0.7}In_{0.3}As$ (1 eV) junction to improve the current matching and increase the device voltage. This triple-junction design is formed by using a $Ga_{0.5}In_{0.5}P/GaAs/Ga_{0.7}In_{0.3}As$ (1eV) solar cell grown on a GaAs substrate and in an inverted order (firstly, $Ga_{0.5}In_{0.5}P$ solar cell). It uses a compositionally graded buffer (CGB) to transition the lattice constant of the $Ga_{0.7}In_{0.3}As$ bottom cell (0.57747 nm) to that of the GaAs substrate (0.565315 nm). Once the complete semiconductor is grown, it is released from the substrate and is turned over using flip-chip processing techniques. Figure 1a shows a schematic of the final solar cell structure. At present, the maximum efficiency achieved using this architecture is 44.4% [5]. The photocurrent of a 1 eV GaInAs inverted metamorphic (IMM) solar cell, as it happens for III-V solar cells, is initially controlled by recombination processes that may occur in the interface between the GaInP window/GaInAs emitter and GaInAs base/GaInP BSF (back surface field), or in the GaInAs active layers. Initially, this last issue, i.e., to achieve high minority-carrier lifetimes, mainly involves two challenges: (i) the design and optimization of the compositionally graded buffer (CGB) to overcome the 2% lattice mismatch between the $Ga_{0.7}In_{0.3}As$ cell and the GaAs substrate [6], and (ii) the $Ga_{0.7}In_{0.3}As$ growth parameters (temperature, V/III, pressure, etc.) to avoid the formation of traps due to vacancies or impurities [7–9].
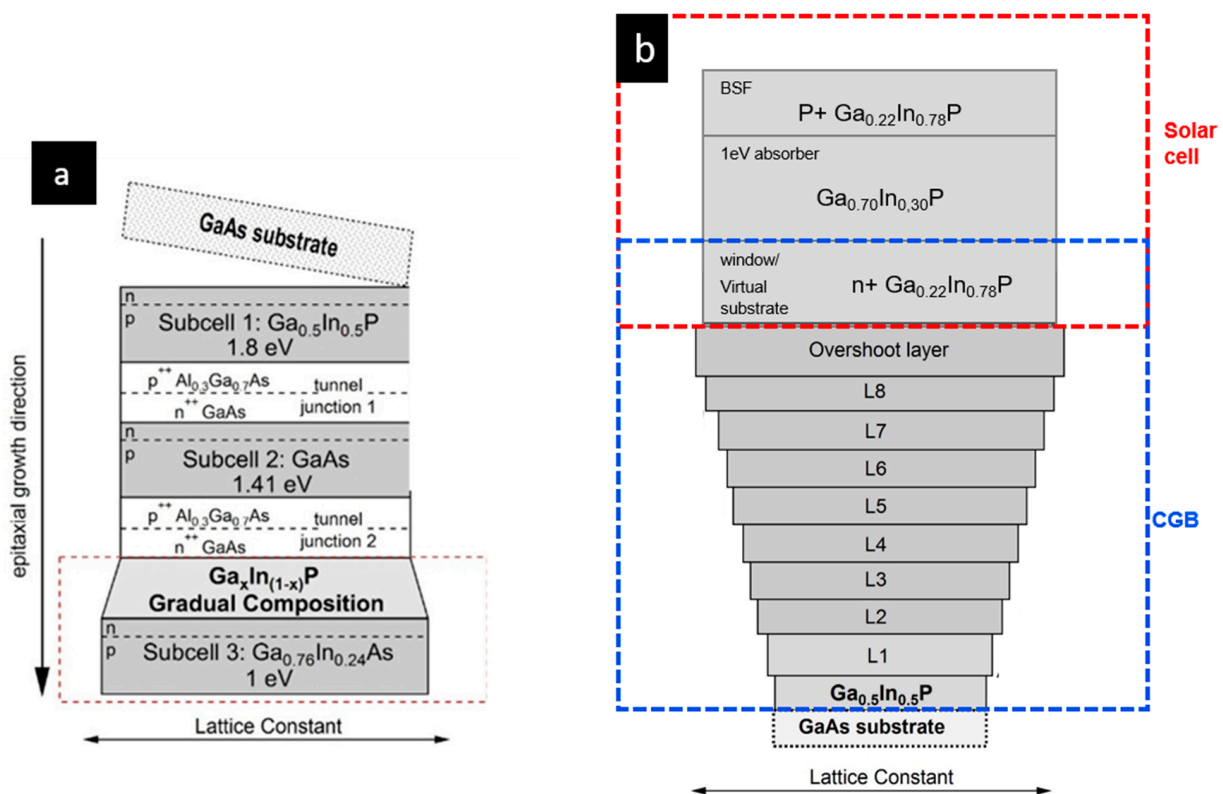

Figure 1. (**a**) Schematic of a $Ga_{0.5}In_{0.5}P/GaAs/Ga_{0.7}In_{0.3}As$ (1 eV) solar cell grown on a GaAs substrate in an inverted order. (**b**) Schematic of the 1 eV GaInAs structure grown using a GaInP compositionally graded buffer (CGB). It is formed by eight n-type 250 nm GaInP steps and an overshoot layer with a 0.25% lattice mismatch. n^{++} and p^{++} stand for very high doped layers.

The features that account for the CGB's quality are the dislocation distribution, threading dislocation density (TDD), and degree of relaxation of each sublayer. The relaxation dynamics during the growth of the CBG dramatically influence the ability to achieve a low residual TDD. The objective is to achieve a maximum relaxation with a minimum number of long misfit dislocations, which are normally placed at the interfaces of the CGB steps. This way, a low-defect and relaxed template can be achieved, with the required lattice constant, to grow a subsequent lattice-matched GaInAs solar cell structure on top. Any residual strain in this template can give rise to further relaxation during the growth of the sub-cell, with the inevitable introduction of misfit dislocations, which possibly occur in the active layers of the structure. Among the possible options, CBGs based on $Ga_xIn_{1-x}P$ are studied in this paper, which provide the required optical transparency and improve TDD reduction due to their atomic ordering [6,10].

Regarding GaInAs solar cells, their photovoltaic (PV) measurement is relatively simple since it is a mono-junction device. However, as described previously, their architecture is composed of several layers with different compositions, which makes it difficult to determine the mechanism governing the quality of the layers involved in the device and, in consequence, to develop a proper feedback strategy. Consequently, the aim of this work is to deeply characterize the semiconductors layers involved in the structure of GaInAs solar cells and to correlate the PV response with the material properties that form the structure.

For this purpose, two 1 eV GaInAs IMM solar cells with different PV behaviors were analyzed. The samples were simultaneously characterized by not only using the most common techniques used for these kinds of structures, such as high-resolution X-ray diffraction (HRXRD) and transmission electron microscopy (TEM), but also using transient in situ surface reflectance and cross-sectional cathodoluminescence (CL) spectra with a 100 nm spatial resolution; to the best of the authors' knowledge, this is the first time that cross-sectional CL was used to characterize these devices. The potential and validation of this technique (cross-sectional CL) have been previously shown for dilute nitrides (GaAsNSb) with a target energy bandgap of 1 eV acting as a sub-cell of a four-junction lattice-matched architecture $GaInP_2/GaAs/1eV/Ge$ [11] and, more recently, for $Cu(In,Ga)Se_2$ solar cells to clarify the mechanism behind the performance improvement of solar cells subjected to a thiourea treatment [12].

The results presented in this work allow the determination of the optimal characterization procedure to evaluate the mechanisms that limit the photovoltaic response of solar cells and, consequently, the development of a more efficient feedback procedure to improve the performance of such devices.

2. Materials and Methods

Both lattice-mismatched 1 eV $Ga_{0.7}In_{0.3}As$ solar cells using $Ga_xIn_{1-x}P$ CGB templates were grown via low-pressure metalorganic vapor-phase epitaxy (MOVPE) on n-GaAs (001) substrates with a misorientation of 2° off toward (111)B, aiming to promote a high single-variant ordering in the GaInP layers, which has demonstrated to enhance dislocation gliding across ordered planes [6].

The CGB structures consist of eight n-type 250 nm GaInP steps with graded compositions, each one with a nominal 0.25% compressive mismatch with respect to the preceding layer; the structures go from $Ga_{0.5}In_{0.5}P$ (lattice matched to GaAs) to $Ga_{0.22}In_{0.78}P$ (lattice matched to $Ga_{0.7}In_{0.3}As$), and then to a final $Ga_{0.20}In_{0.80}P$ overshooting layer. A nominally fully relaxed $Ga_{0.22}In_{0.78}P$ layer was deposited afterward. This acts as a virtual substrate (crystallographic template) for the subsequent strain-free growth and as the front passivation layer of the metamorphic solar cell (window layer). Figure 1b shows the as-grown GaInAs 1 eV solar cell structure analyzed in this work.

The CGB of both structures was grown at 675 °C, with a high V/III ratio (V/III = 65) and a high growth rate, to reduce the crosshatch roughness and promote the dislocation gliding, aiming to minimize the TDD [10]. However, the growth of each CGB differed in the strategy used to build the steps and the final relaxation provided by the overshoot

layer. Sample #1 used a constant growth rate of 8 μm/h by simultaneously changing the flows of TMGa and TMIn to attain the target compositions at each step. Conversely, Sample #2 used a linear variation in the growth rate, starting at 4.5 μm/h and finishing at 7.5 μm/h, by keeping the TMIn flow constant and reducing the TMGa at each step. This latter method allows more abrupt composition changes between steps, but, due to hardware range limitations, the growth rates are lower on average, which has an impact on CGB relaxation. Additionally, Sample #1 has a 1 μm thick overshoot, while in Sample #2, the overshoot is 500 μm thick. The thickness of the overshoot influences the final relaxation of the CGB and the strain state of the final window layer.

Regarding the GaInAs solar cells, they are based on a 0.1-μm n-type emitter and a 3-μm p-type base, with doping levels of $1 \cdot 10^{18}$ and $1 \cdot 10^{17}$ cm^{-3}, respectively. In both samples, the solar cells were grown at 5 μm/h with a V/III of 20, although the growth temperature for the GaInAs solar cell of Sample #1 was 640 °C, while for Sample #2, the temperature was 675 °C. The chamber pressure was also different for both samples, which changed the partial pressure of the constituents. These growth parameters are summarized in Table 1. On another note, in Sample #1, the final 500 nm of the window layer was grown by shifting the growth temperature from 675 °C to 640 °C, which is the temperature used for the deposition of the GaInAs layers. This fact brings additional implications. For instance, since the incorporation of group III elements in the lattice depends on the growth temperature, a compositional grading can be expected.

Table 1. Growth parameters of GaInP compositionally graded buffer and GaInAs cell for Sample #1 and Sample #2.

		Sample #1	Sample #2
GaInP CGB	Growth temperature (°C)	675	675
	V/III ratio	65	65
	Growth rate (μm/h)	4.5 to 7.5	8
	Overshoot thickness (μm)	1	0.5
GaInAs	Growth temperature (°C)	640	675
	V/III ratio	20	20
	Growth rate (μm/h)	5	5
	Pressure	250 mbar	100 mbar

The complete 1 eV solar cells were characterized by means of external quantum efficiency (EQE) carried out using a custom-made system based on an Xe lamp and a grating monochromator.

The composition and strain of the GaInAs layer and the steps of the GaInP CGB were measured via high-resolution X-ray diffraction using a Panalytical X-pert Pro diffractometer from Malver Panalytical (Malver, United Kingdom), using Cu Kα1 radiation. The strain of the CGB layers were determined by analyzing the reciprocal space maps (RSMs) of the symmetric (004) and asymmetric (224) reflections with the X-rays incident in the (110) plane. For TEM characterization, the structures were thinned up using a focused ion beam (FIB) lift-out procedure. The samples were prepared in the two orthogonal [110] and [1–10] directions in order to unambiguously investigate the CuPt ordering existing in the layers. A Philips Tecnai F20 transmission electron microscope from Thermo Fishser (Waltham, MA, USA) operated at 200 kV with a scanning transmission (STEM) module and a high-angle annular detector (HAAD) for Z-contrast imaging was used to study the microstructure and CuPt ordering. The selected area electron diffraction (SAED) was used to determine the existence of atomic order in the different sublayers. The band gap energy across the GaInAs layer was measured by means of cross-sectional spectral CL using a MonoCL2 from Gatan (Pleasanton, CA, USA) system attached to a LEO 1530 field-emission scanning electron microscope (FE-SEM) from Georgia Tech, (Atlanta, GA, USA). The detection of spectrally resolved CL was performed using a liquid-nitrogen-cooled GaInAs array detector (800–1700 nm spectral range). The CL spectra were sequentially

collected along the growth direction by scanning in steps of $\approx$ 100 nm. The CL spectra were obtained at 80 K in order to improve the signal-to-noise ratio and at 5 kV with a lateral resolution of around 120 nm. The main peak for each spectrum was identified as the near-band-edge (NBE) emission, which follows a similar evolution to the band gap. Additionally, the in situ monitoring tool EpiRas 2000 from Laytec (Berlin, Germany) was used to acquire the transient in situ surface reflectance during the process of epitaxy using a monochromatic light source of 2.1 eV.

3. Results

3.1. External Quantum Efficienty

Figure 2 shows the external quantum efficiency (EQE) measurements of Sample #1 and Sample #2. A difference in the composition of the $Ga_xIn_{1-x}As$ absorber layers can be inferred from the EQE cutoff wavelength. This was verified using the HRXRD measurements, obtaining a composition of x = 0.71 for Sample #1, and x = 0.695 for Sample #2. These compositions correspond to a band gap energy of 1.018 eV (λ = 1218 nm) for Sample #1 and 0.995 eV (λ =1245 nm) for Sample #2, both at 300 K. This implies a difference of ΔEgap = 23 meV in the band gap energy between the two samples, which is consistent with the EQE measurements.
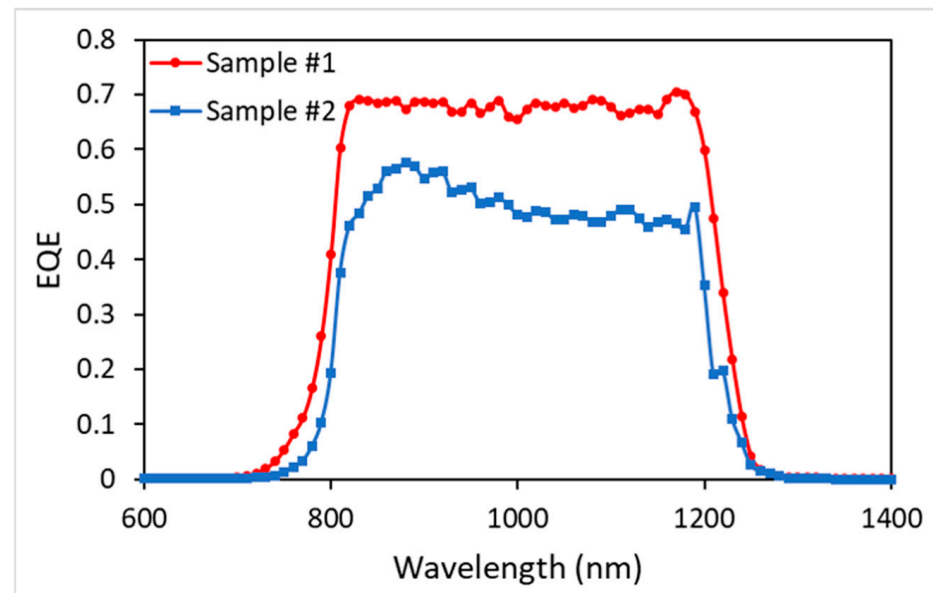

Figure 2. External quantum efficiency of 1 eV GaInAs inverted metamorphic solar cells for Sample #1 and Sample #2.

Figure 2 reveals a global decrease in the EQE curve for Sample #2. Two-dimensional numerical simulations using Silvaco TCAD ATLAS were carried out to reproduce the experimental EQE data assuming (a) a variation in the minority-carrier lifetime (τ_{bulk}) of the 1 eV absorber ($Ga_{0.70}In_{0.30}As$), (b) a variation in the interface recombination velocity (IRV) for the emitter–window interface, and (c) a variation in the interface recombination velocity (IRV) for the base–BSF interface.

The minority-carrier lifetimes were calculated using Equation (1):

$$\frac{1}{\tau_{bulk}} = \frac{1}{\tau_{SRH}} + \frac{1}{\tau_{Auger}} + \frac{1}{\tau_{rad}} \tag{1}$$

where τ_{SRH} is related to the Shockley–Read–Hall recombination, which depends on the existing bulk defects; τ_{Auger} is the Auger recombination via a three-particle process; and τ_{rad} is the intrinsic or radiative recombination via a band-to-band process. For the experimental data fitting, τ_{SRH} was varied, while τ_{Auger} and τ_{rad} were set to the common values for this

type of material system, i.e., Auger and radiative coefficients being equal for electrons and holes, with values of 10^{-30} cm^3/s and 10^{-10} cm^3/s, respectively.

Figure 3a shows the simulated EQE for different τ_{bulk}, considering fixed emitter–window and base–BSF interfaces with an average IRV of $1 \cdot 10^6$ cm/s. The simulated data accurately reproduce the experimental EQE curves, revealing a shape tendency equivalent to the Sample #2 data for τ_{bulk} lower than $5 \cdot 10^{-9}$ s. More precisely, τ_{SRH} is fitted to $5 \cdot 10^{-8}$ s or higher for Sample #1 and to $5 \cdot 10^{-10}$ s for Sample #2, which corresponds to a minority-carrier diffusion length (L_d) of 9.8 μm and 0.4 μm, respectively. It is important to remark that for Sample #1, τ_{bulk} may be controlled by τ_{rad} instead of τ_{SRH}. Conversely, for Sample #2, due to the existence of a higher number of bulk defects, the Shockley–Read–Hall recombination can be assumed to be the dominant process. Consequently, the simulations reveals that the differences observed between the two samples might be related to the GaInAs quality, as the EQE of Sample #2 can be easily reproduced by tuning (reducing) the minority-carrier lifetime of the active layer.
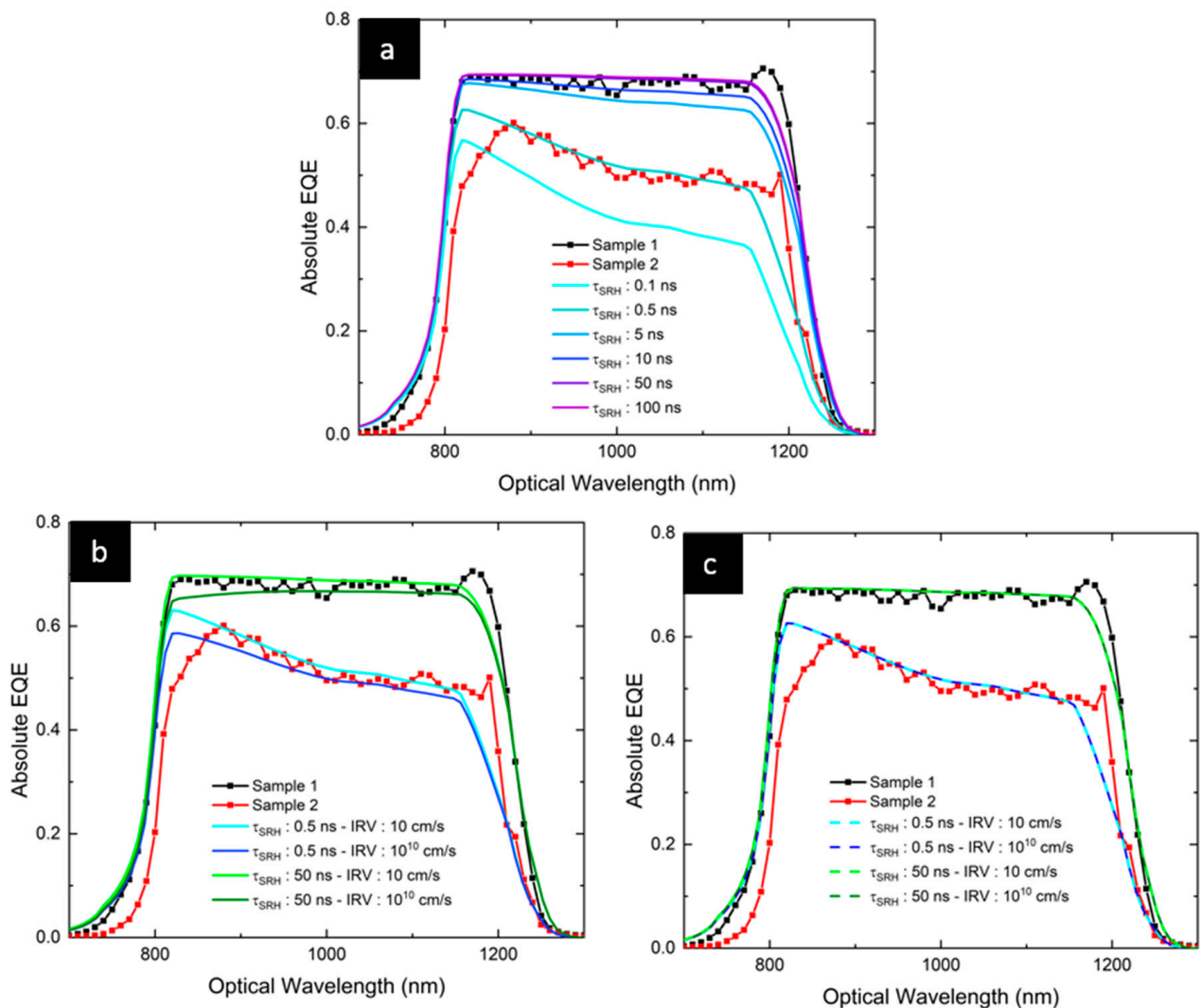

Figure 3. Silvaco TCAD ATLAS numerical simulations of a 1 eV GaInAs solar cell's EQE: (**a**) varying the bulk SRH lifetimes with fixed emitter–window and base–BSF interfaces with an average IRV of $1 \cdot 10^6$ cm/s; (**b**) window–emitter interface recombination velocities (IRV) for τ_{SRH} equal to $5 \cdot 10^{-8}$ and $5 \cdot 10^{-10}$s; and (**c**) base–BSF interface recombination velocities (IRV) for τ_{SRH} equal to $5 \cdot 10^{-8}$ and $5 \cdot 10^{-10}$s.

In addition, to determine to what extent the emitter–window and/or base–BSF interface quality is responsible for the EQE degradation measured in Sample #2, Figure 3b,c show the simulated EQE dependence with the emitter–window IRV and base–BSF IRV, respectively, ranging from a high-quality interface (IRV = 10 cm/s) to an interface with a high recombination rate (IRV = 10^{10} cm/s). The EQE values were simulated by fixing τ_{SRH} to the previously fitted bulkcarrier lifetimes of $5 \cdot 10^{-8}$ and $5 \cdot 10^{-10}$ s in both cases. It is clearly seen that the impact of both interfaces on the simulated EQE is almost negligible for a fixed value of τ_{SRH}.

This result is due to the difference between the band gap of the $Ga_{0.22}In_{0.78}P$ window and the BSF layers ($\approx$1.50 eV) and the band gap of the GaInAs cell active material ($\approx$1 eV), together with an optimal band alignment. The resultant conduction and valance bands are shown in Figure 4a. It creates high electric fields both in the proximity of the interfaces formed by the window–emitter and the base–BSF (both shown in Figure 4b), which drastically reduce the impact of the quality of the interfaces on the carrier collection.
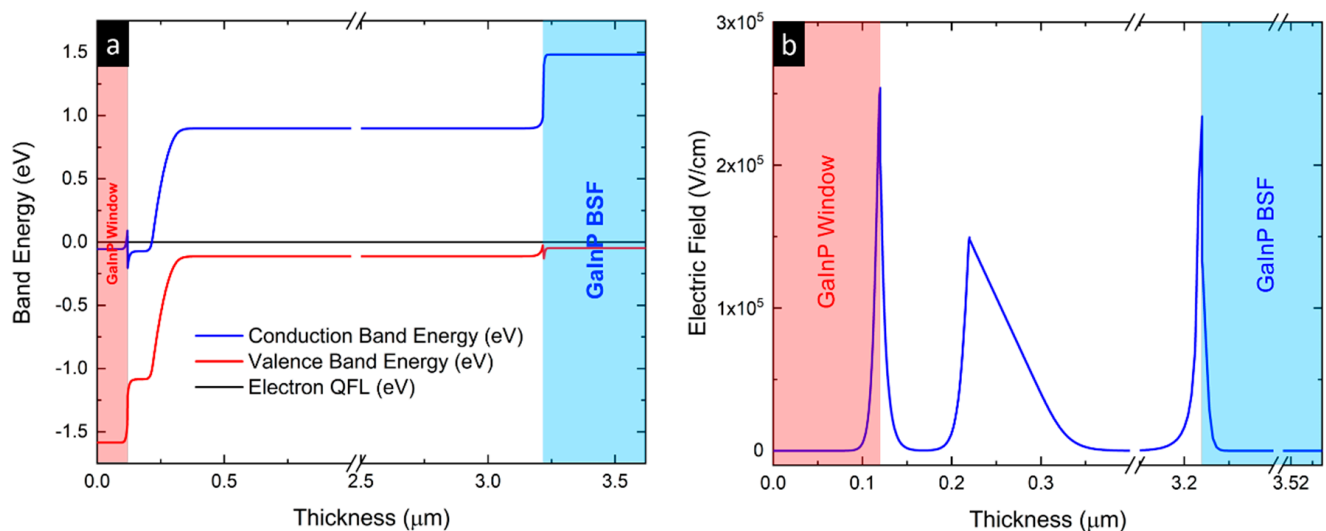

Figure 4. (**a**) Band structure for the 1 eV GaInAs solar cell at equilibrium (0 V), and (**b**) total electric field module in the vicinity of the window–emitter (right) and base–BSF (left) interfaces. All values were simulated using Silvaco TCAD ATLAS.

Consequently, the limiting factor in the PV response for 1 eV GaInAs inverted metamorphic solar cells with GaInP as the window and BSF layers is the minority-carrier lifetime.

As mentioned before, the reason behind the deterioration of minority-carrier properties can be due to mainly two reasons: (i) the formation of threading dislocations due to plastic deformation, and (ii) the presence of traps due to vacancies or impurities related to the GaInAs growth conditions. In order to feedback the device fabrication, a deep characterization study using multiple characterization techniques was carried out.

3.2. High-Resolution X-ray Diffraction

The reciprocal space maps (RSMs) of the symmetric (004) and asymmetric (224) reflections achieved via XRD were used to calculate the strain for each GaInP sublayer. Figure 5 shows the reciprocal space map (RSM) measurements of the CGB of the two samples before and after growing the GaInAs sub-cell on top.
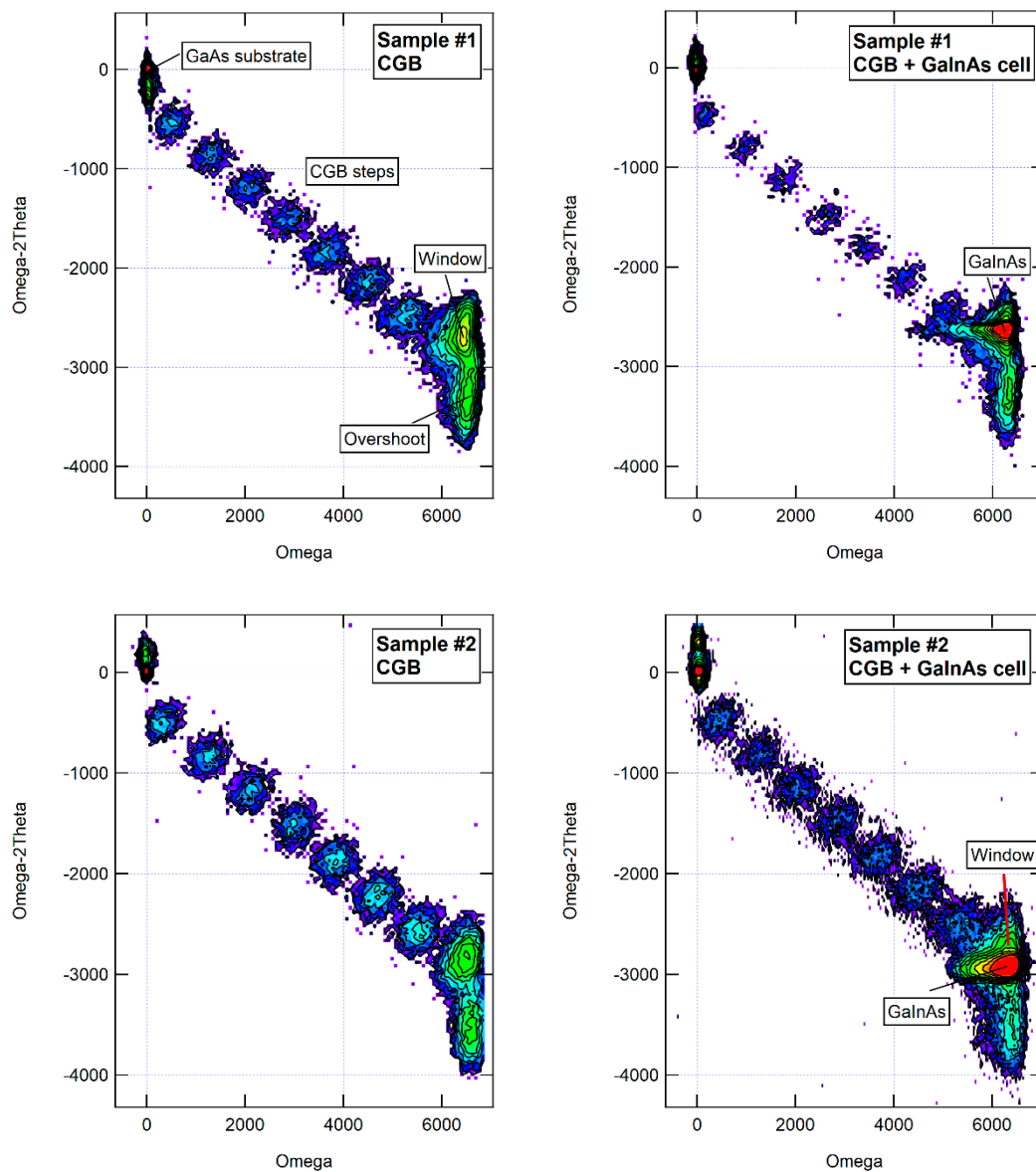
Figure 5. Reciprocal space maps of the CGB and CGB plus GaInAs cell structures for Sample #1 and Sample #2 taken around the 004 reflection along the [1–10] direction. The typical tilt observed in ordered GaInP CGBs can be seen.

The structural parameters extracted from the RSMs (i.e., composition and residual strain) of the window and GaInAs layers are presented in Table 2.

Table 2. Structural parameters of the GaInP window and GaInAs layers of Sample #1 and #2.

	Sample #1	Sample #2
Window composition	$Ga_{0.23}In_{0.77}P$	$Ga_{0.22}In_{0.78}P$
Window in-plane lattice constant (A)	5.773	5.777
Window residual strain (%)	0.001	−0.044
GaInAs composition	$Ga_{0.71}In_{0.29}As$	$Ga_{0.69}In_{0.31}As$
GaInAs in-plane lattice constant (Armstrong)	5.771	5.779
GaInAs elastic strain (%)	0.014	−0.122

Significant differences are observed. Focusing on the effect of the GaInAs sub-cell growth, it can be observed there is a shift in Omega-2Theta between the window and the GaInAs layer for Sample #2. This fact reveals a lattice mismatch between the window and the GaInAs layer (see Table 2). Note that the RSM shown provides a picture of the relaxation and strain at the end of growth, but no precise information about the evolution of these parameters during the growth process can be obtained unless an in situ curvature measurement is used. Additionally, an Omega-2Theta broadening of the GaInAs peak is observed in Sample #2. This result also supports the idea of relaxation during growth through the introduction of dislocations. Finally, the residual strain obtained from the full set of RSMs taken using symmetric (004) and asymmetric (224) reflection measurements (not shown) indicates a value of 0.014% (tensile) for Sample #1 and −0.122% (compressive) for Sample #2. The tensile residual strain observed is another evidence supporting a relaxation of the GaInAs layer via the introduction of dislocations. According to [13], inverted metamorphic 1 eV GaInAs solar cells show good performance over a relatively wide range near zero stress and slightly compressive stress, but degrade quickly under tension, which is consistent with our PV results.

3.3. Transmision Electron Microscopy

TEM characterization was carried out on Sample #1 and Sample #2. Figure 6 shows the [011] dark-field cross-sectional images, confirming the existence of defects in the GaInAs layers of Sample #2 (mainly stacking faults and threading dislocations), while the density of defects in Sample #1 is below the measurements area of the TEM micrograph, thus strengthening the previous conclusion, i.e., a tensile layer promotes the formation of TDD.
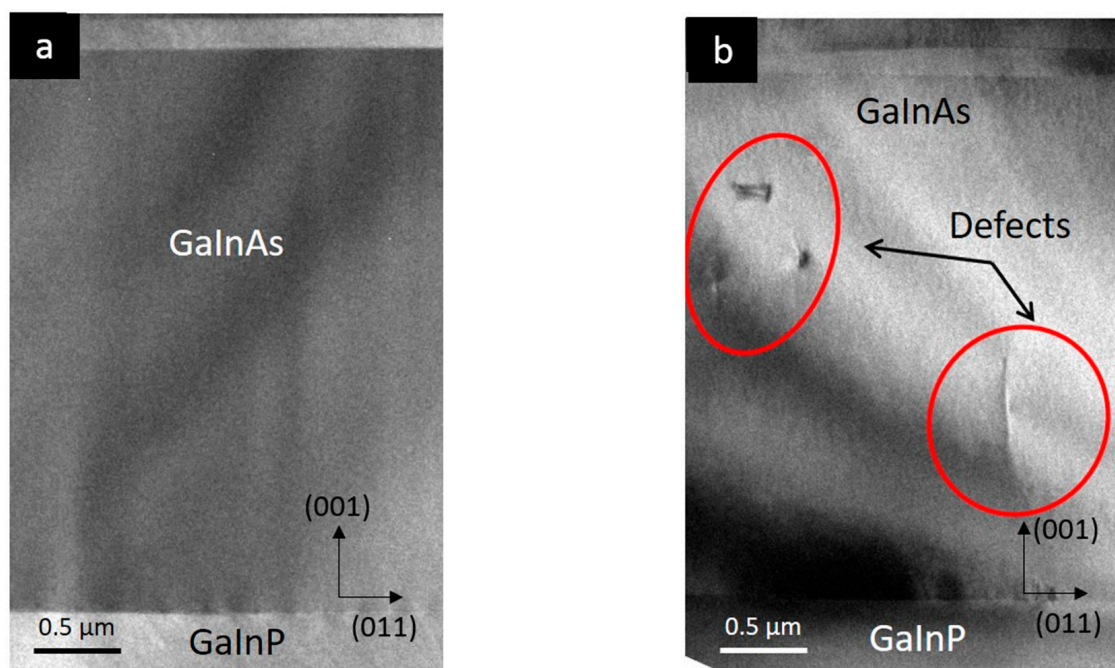

Figure 6. Cross-sectional [011] dark-field TEM images in the [110] zone axis of (**a**) Sample #1 and (**b**) Sample #2.

Selection area electron diffraction (SAED) was carried out on the layers of both samples. Specifically, the crystallographic order in the GaInAs layer and in the GaInP overshoot layer (last layer of the compositionally graded buffer, Figure 1b) was analyzed to correlate it with the difference in threading dislocations between the samples.

As shown in Figure 7a,b, it can be observed there are $1/2\{111\}$ diffraction spots which are related to CuPt GaInP ordering, as has been widely reported [4]. Additionally, it is observed that in Sample #1, the spots are rounder and lighter, which could imply a more

homogeneous layer with a lower degree of phase separation and a lower order degree than in Sample #2. According to [4], atomic ordering strongly influences the glide plane distribution in lattice-mismatched systems, which could explain the higher density of defects in Sample #2. The difference in the degree of atomic ordering between the samples is most likely related to the growth rate used for each CGB (Table 1).
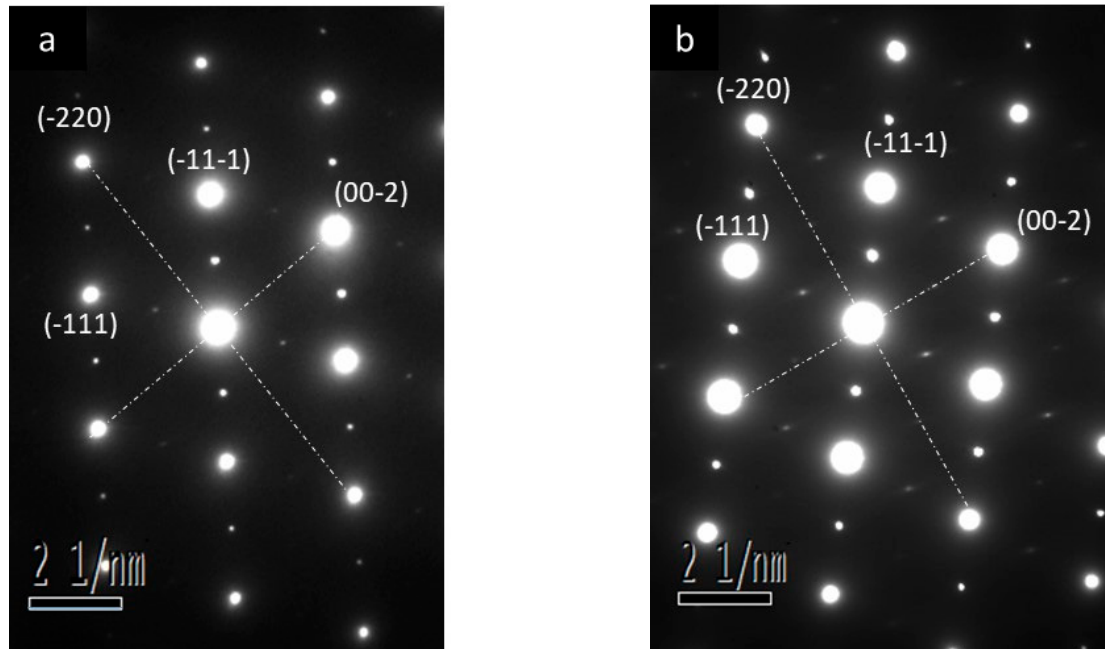

Figure 7. SAED in the [110] zone axis of the GaInP overshoot layer of (**a**) Sample #1 and (**b**) Sample #2.

3.4. Cross-Sectional Catholuminiscence and In Situ Reflectance Spectroscopy

Cross-sectional CL was carried out. This technique is a powerful tool to analyze the band gap energy through the layers and to study possible compositional fluctuations [9] and defects across the GaInAs layers. The measurements were taken at 80 K along the growth direction of each GaInAs layer using steps of around 100 nm (Figure 8). Figure 8a,b show the spectra for Sample #1 and Sample #2, respectively. Figure 8c shows the punctual CL spectra measured at 1000 nm from the surface for the two samples, which have been normalized to their maximum intensity. In Figure 8d, the two spectra are energy shifted to be overlapped for an easier observation of the peak´s shape.

The first conclusion drawn from the CL measurements is that the band gap energy values are stable across the structure for both samples, indicating that the GaInAs layers do not present macroscopic compositional fluctuations. By analyzing the data, it is observed that there is a shift to higher energies for Sample #1 (1.0190 $\pm$ 0.0002 eV at 80K) (0.95 at 300 K) with respect to Sample #2 (0.9899 $\pm$ 0.0003 eV at 80K) (0.92 at 300K), which corresponds to a difference ΔE_{gap} = 29.1 $\pm$ 0.5 meV in the band gap energy between the samples. This band gap energy shift can be attributed to three factors: composition, strain, and ordering. The difference in the band gap energy between the samples related to composition variations was calculated before using HRXRD, showing ΔE_{gap} = 23 meV. The strain factor was obtained using the HRXRD measurements. The calculated residual strain values are small for both samples, i.e., −0.01% for Sample #1and 0.12% for Sample #2, resulting in a band gap energy difference of ΔE_{gap} = 6 meV due to strain [14]. Finally, the ordering factor was discarded since no ordering was found in both GaInAs layers based on the electron diffraction patterns. Therefore, it can be claimed that the band gap energy shift can be mainly ascribed to a change in composition between the samples, which is consistent with previous results.
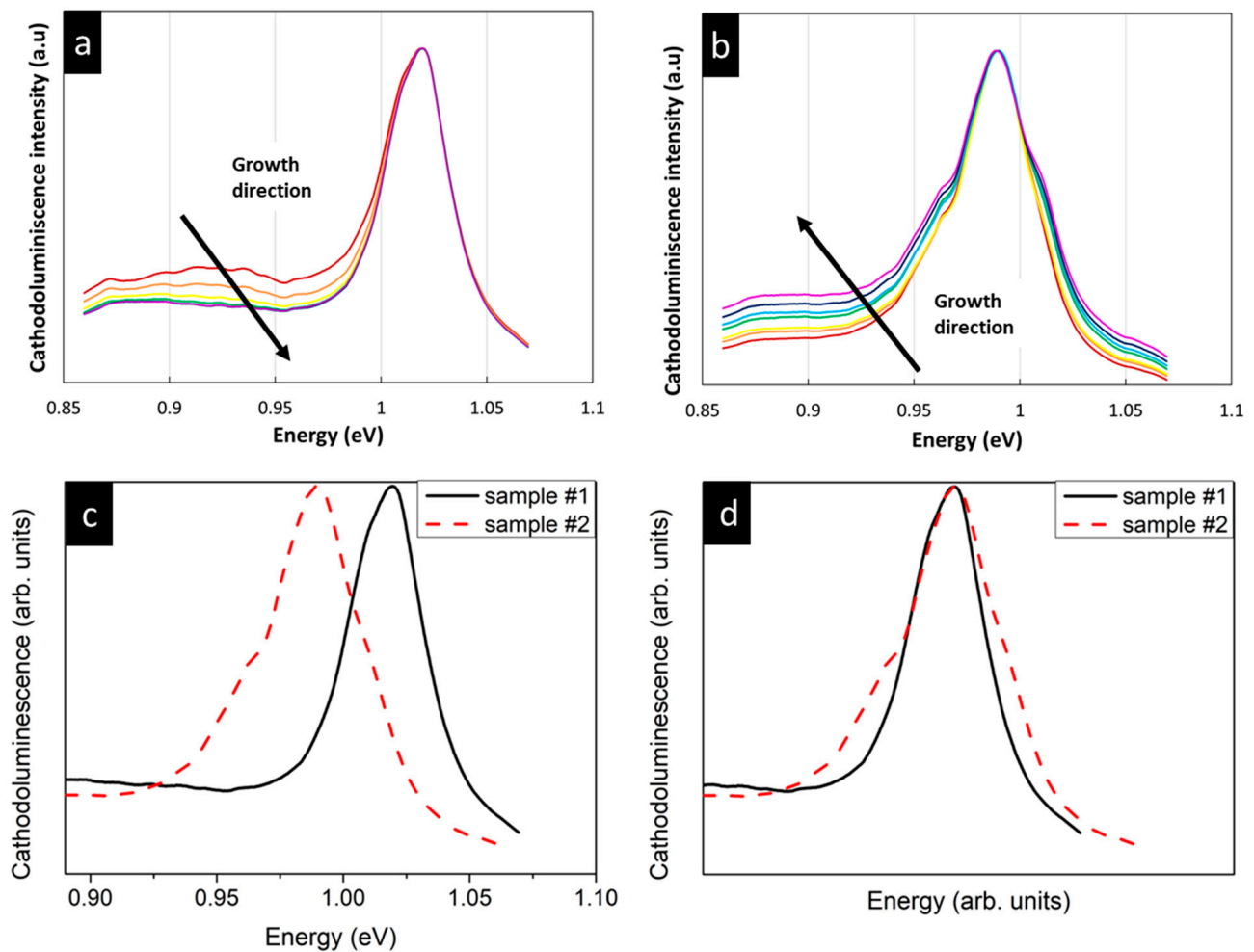
Figure 8. Cross-sectional CL spectra of the GaInAs layer along the growth direction (marked with an arrow) for Sample #1 (**a**) and Sample #2 (**b**). The set of spectra for each sample follows the colors of the rainbow, being red for the first one and purple for the last one. Comparison of punctual CL spectra of the GaInAs layer measured at 1000 nm from the surface (**c**) and shifted in energy (**d**). Each spectrum was normalized to its maximum intensity. The data were achieved at 80 K.

The broadening observed in Sample #2 (Figure 8d) reveals a poorer crystal quality, which agrees with the results obtained using the TEM and the EQE simulation data. Additionally, the fact that this broadening appears at a certain depth from the beginning of the layer (Figure 8b) disputes that the existence of traps due to impurities or vacancies is responsible for the lower GaInAs minority-carrier lifetime of Sample #2. Conversely, it confirms the formation of dislocations and defects due to lattice mismatch between the layers as being the main cause of the deterioration in material quality. This hypothesis can also be verified using the evolution of transient in situ surface reflectance during the deposition of the GaInAs layer, as shown in Figure 9.

It corroborates the deterioration in the GaInAs layer of Sample #2 since the in situ surface reflectance signal drops after the deposition of about 1500 nm of GaInAs, whilst the signal stays constant during the complete GaInAs growth of Sample #1. This drop points to surface degradation that is most likely related to strain relaxation. In addition, it is worth noting that this behavior is consistent with the broadening of the CL spectra of Sample #2 after a certain depth (Figure 8b).
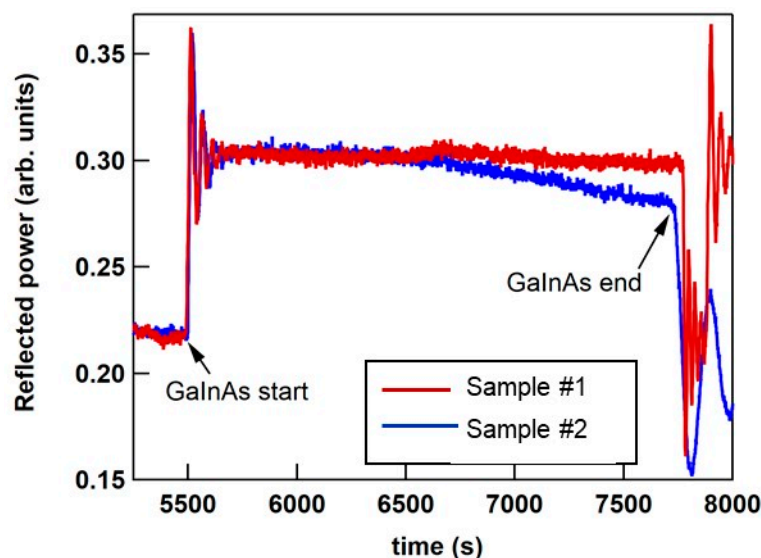
Figure 9. Transient in situ surface reflectance measured at 2.1 eV during the deposition of the GaInAs layer. Red line corresponds to Sample #1 and blue line corresponds to Sample #2.

4. Discussion and Conclusions

Deep characterization of 1 eV GaInAs inverted metamorphic solar cells, together with a simulation process of the EQE measurements, was carried out to correlate the PV response of the complete device with the structural properties of the different semiconductor layers involved in the structure to achieve a deeper understanding of the mechanism limiting their improvement. Silvaco TCAD ATLASs was used to reproduce the experimental EQE measurements, showing that the reduction in the EQE of Sample #2 is related to a low minority-carrier lifetime since the recombination velocities in the window–emitter and/or in the base–BSF interface are not influenced due to a favorable alignment between the conduction and the valance bands. The minority-carrier lifetime can be theoretically modulated by the presence of structural defects linked to strain relaxation or traps; the latter are due to impurities or vacancies related to the growth conditions. The cross-sectional cathodoluminescence, together with transient in situ surface reflectance, disputed the GaInAs growth conditions as being responsible for the decrement in the minority-carrier lifetime. Conversely, the TEM and HRXRD characterization revealed that the misfit dislocations in Sample #2 were formed during the growth of the GaInAs layer due to a high elastic strain, which was probably due to an excessive tensile strain in the virtual substrate or an incorrect combination of alloy compositions in the topmost layers; this was the dominant factor for the deterioration in the GaInAs layer, which worsened the PV response.

Consequently, it can be concluded that the potential of each characterization technique used has been revealed, which allows the detection of the weak points of semiconductor structures. This information is highly relevant when deciding which aspects need a greater improvement effort.

Author Contributions: Conceptualization, B.G. and A.N.; software, D.M.-M.; validation, B.G., A.N., M.H., I.G. and J.J.; formal analysis, B.G., A.N., M.H. and I.G.; investigation, B.G., A.N., M.H., I.G. and J.J.; resources, B.G., A.N., M.H., I.G. and J.J.; data curation, B.G., A.N., M.H. and I.G.; writing—original draft preparation: B.G. and A.N.; writing—review and editing: M.H., I.G. and E.G.-T.; visualization, B.G., A.N., M.H., I.G., D.M.-M. and E.G.-T.; supervision B.G.; project administration, B.G.; funding acquisition, B.G., I.G. and D.M.-M. All authors have read and agreed to the published version of the manuscript.

Data Availability Statement: The raw/processed data required to reproduce these findings cannot be shared at this time due to technical or time limitations.

Conflicts of Interest: The authors declare no conflict of interest.

References

1. King, R.R.; Boca, A.; Hong, W.; Liu, X.; Bhusari, D.; Larrabee, D.; Edmondson, K.M.; Law, D.C.; Fetzer, C.M.; Osterwald, C.; et al. Band-Gap-Engineered Architectures for High-Efficiency Multijunction Concentrator Solar Cells. In Proceedings of the 24th European Photovoltaic Solar Energy Conference, Hamburg, Germany, 21–25 September 2009; pp. 21–25.
2. Olson, J.M.; Kurtz, S.R.; Kibbler, A.E.; Faine, P. A 27.3% efficient $Ga_{0.5}In_{0.5}P$/GaAs tandem solar cell. *Appl. Phys. Lett.* **1990**, *56*, 623–625. [CrossRef]
3. France, R.M.; Geisz, J.F.; Olavarria, W.; Young, M.; Kibbler, A.; Steiner, M.A. Triple-junction solar cells with 39.5% terrestrial and 34.2% space efficiency enabled by thick quantum well superlattices. *Joule* **2022**, *6*, 1121–1135. [CrossRef]
4. Geisz, J.F.; France, R.M.; Schulte, K.L.; Norman, A.G.; Guthrey, H.L.; Young, M.R.; Song, T.; Moriarty, T. Six-junction III–V solar cells with 47.1% conversion efficiency under 143 Suns concentration. *Nat. Energy* **2020**, *5*, 326–335. [CrossRef]
5. Sasaki, K.; Agui, T.; Nakaido, K.; Takahashi, N.; Onitsuka, R.; Takamoto, T. Development Of InGaP/GaAs/InGaAs inverted triple junction concentrator solar cells. *AIP Conf. Proc.* **2013**, *1556*, 22–25. [CrossRef]
6. France, R.M.; McMahon, W.E.; Romero, M.J. Control of misfit dislocation glide plane distribution during strain relaxation of CuPt-ordered GaInAs and GaInP. *J. Appl. Phys.* **2012**, *112*, 023520. [CrossRef]
7. Brozel, M.R.; Gregory, E. (Eds.) *Properties of Gallium Arsenide (EMIS Datareviews, 16)*; Institute of Engineering & Technology, Stillman College: Tuscaloosa, AL, USA, 1996.
8. Kuech, T.F.; Veuhoff, E. Mechanism of carbon incorporation in MOCVD GaAs. *J. Cryst. Growth* **1984**, *68*, 148–156. [CrossRef]
9. Takagishi, S.; Mori, H. Epitaxial Growth of High-Purity GaAs by Low-Pressure MOCVD. *Jpn. J. Appl. Phys.* **1984**, *23*, L100. [CrossRef]
10. France, R.M.; Geisz, J.F.; Steiner, M.A.; To, B.; Romero, M.J.; Olavarria, W.J.; King, R.R. Reduction of crosshatch roughness and threading dislocation density in metamorphic GaInP buffers and GaInAs solar cells. *J. Appl. Phys.* **2012**, *111*, 103528. [CrossRef]
11. Navarro, A.; Martinez, O.; Galiana, B.; Lombardero, I.; Ballesteros, C.; Jimenez, J.; Algora, C. Cathodoluminescence characterization of the bandgap energy in dilute nitride GaNSbAs alloys. *J. Electron. Mater.* **2018**, *47*, 5061–5067. [CrossRef]
12. Nakada, K.; Nishimura, T.; Suyama, N.; Yamada, A. Cathode luminescence analysis of $Cu(In,Ga)Se_2$ solar cells treated with thiourea solution. *Jpn. J. Appl. Phys.* **2021**, *60*, 031001. [CrossRef]
13. Geisz, J.F.; Levander, A.X.; Norman, A.G.; Jones, K.M.; Romero, M.J. In situ stress measurement for MOVPE growth of high efficiency lattice-mismatched solar cells. *J. Cryst. Growth.* **2008**, *310*, 2339–2344. [CrossRef]
14. Zakaria, A.; Fetzer, C.M.; Goorsky, M.S. Influence of the degree of order of InGaP on its hardness determined using nanoindentation. *J. Appl. Phys.* **2010**, *108*, 074908. [CrossRef]